

Local Flame Structure and Turbulent Burning Velocity by Joint PLIF Imaging

by

Kazuhiro YAMAMOTO, Shinji ISII, and Masahiro OHNISHI

Department of Mechanical Science and Engineering, Faculty of Engineering, Nagoya University
Furo-cho, Chikusa-ku, Nagoya-shi, Aichi 464-8603, JAPAN

(Abstract)

In this study, we have examined local flame structure by joint PLIF imaging, using simultaneous OH/HCHO-PLIF and orthogonal OH-PLIF measurements. By considering the degree of flame wrinkling, three-dimensional flame surface area is obtained from 2D images. We have used a cyclone-jet combustor to establish turbulent premixed flames for propane/air mixtures in a wide range of turbulence, covering the flamelet regime and thin reaction zones regime on combustion diagram. Results show that as the mean velocity at the combustor exit is increased, more complex flame structure is observed with multiple flamelets. Near the global extinction, peak OH concentration in reaction zone becomes almost zero whereas HCHO concentration in preheat zone still remains. As a result, the large reduction of heat release rate occurs, resulting in local extinction. The turbulent burning velocity determined by the mean flame shape is increased with turbulence, and the bending effect is observed in thin reaction zones regime. On the other hand, different from the flame perimeter, the flame surface area is linearly increased. Since the turbulent burning velocity is well predicted by the classical formula in wrinkled flames, the bending is explained by the reduction of local burning velocity. Thus, within the frame work in our measurement, the flamelet approach could be still valid even in the thin reaction zones regime.

Introduction

So far, for modeling turbulent combustion, numerous studies have been made [1-6]. It is considered that the turbulence intensifies the fuel consumption rate due to the increased heat and mass transfer, compared with laminar combustion. As for the turbulent burning velocity, Damköhler [1] has proposed that, when the flame only wrinkles with turbulence, the turbulent burning velocity, S_T , is expressed by

$$S_T = (A_T / A_L)S_L \quad (1)$$

where A_T is the surface area of the wrinkled flame front, A_L is the cross-sectional area of the front projected in the direction of flame propagation, and S_L is the laminar burning velocity. Although this classical hypothesis has very simple formula, the idea is adopted in numerical models [6]. Based on this equation, the turbulent burning velocity is intensified with turbulence due to the increase of the flame surface area. However, there is a certain level of turbulence at which combustion is maintained. In reality, turbulent burning velocity is not monotonically increased with turbulence, which is called bending. The local quenching could occur under highly turbulent condition [7-9]. Many studies focusing on laminar flames have been conducted to show that the local quenching is caused by the strain, curvature, and heat loss [10,11].

To discuss the flame structure, a phase diagram is useful [2,3,6]. If the turbulence is relatively low, the local flame structure is that of a laminar flame with wrinkled flame front. However, in high intensity of turbulence, it has been proposed that the reaction zone is still thin with thickened preheat zone in thin-reaction-zones regime [3]. Then, the turbulent burning velocity predicted by Eq. 1 has not been well validated, especially in the thin reaction zones regime. It is argued that the flame propagation speed is much higher than the laminar burning velocity in this regime. Recent measurement has reported that its value is much smaller than the laminar burning velocity [12]. On the other hand, it is difficult to obtain the flame

surface area by laser diagnostics of 2D imaging, and some advanced approaches have been proposed [13-15]. Thus, the further study is needed to investigate the turbulent burning velocity based on both the local burning velocity and flame surface area [16].

In this study, the local flame structure is visualized by joint PLIF technique. In order to evaluate the flame surface area by 2D LIF imaging, two approaches are applied. One is the simultaneous OH and HCHO fluorescence imaging to evaluate the heat release rate [17-19]. The other is the orthogonal OH-PLIF measurement to obtain the 2D images in both the vertical and horizontal planes, which is quite a new trial for further discussion on 3D flame structure. The turbulent premixed flames are formed by a cyclone-jet combustor in a wide range of turbulence [20-22]. It should be noted that the flame characteristics including local burning velocity could be examined based on peak OH concentration in turbulent flames [23]. Then, focusing on OH as well as HCHO, we discuss the local flame structure and turbulent burning velocity.

Experimental setup

Cyclone-jet combustor

Figure 1 shows a cyclone-jet combustor (C-J combustor). It consists of a combustion chamber with a main jet nozzle and two cyclone nozzles for pilot flames. The diameter of the main jet nozzle is 12.7 mm and that of the cyclone combustor is 21 mm, with two cyclone nozzles of 2.4 mm i.d. Due to a circular pilot flame inside the combustor, the flame is stabilized at the combustor exit, and hence, it is easy to obtain the flame image by PLIF. In the experiment, we varied the mean exit velocity, U_m , and the equivalence ratio, ϕ_m , of the main jet, with a fixed condition of pilot flames for $U_p = 20$ m/s and $\phi_p = 0.7$. The fuel is propane. In our previous measurements by LDV and PIV, the turbulent Reynolds number, Re_T , is from 96 to 448 for $U_m = 5$ to 30 m/s, $\phi_m = 0.75$ and 0.9 [20,21]. On the phase diagram, the condition of $U_m < 15$ m/s for $\phi_m = 0.75$ or $U_m < 20$ m/s for $\phi_m = 0.90$ belongs to the flamelet regime, and that of $U_m > 20$ m/s for $\phi_m = 0.75$ or $U_m = 30$ m/s

Fig.1

for $\phi_m = 0.90$ belongs to the thin reaction zones regime. The flame is completely extinguished slightly above 30 m/s at $\phi_m = 0.75$. Before that, the global quenching [9] does not occur.

Typically, an imaging area by PLIF is at $Z = 13.75$ to 26.25 mm and $Y = -7.5$ to 17.5 mm, where Z represents the axial distance from the combustor exit and Y is the horizontal axis.

OH/HCHO PLIF system

The experimental setup for PLIF system is shown in **Fig. 2**. As for the simultaneous OH and HCHO fluorescence imaging, two laser sheets were used to excite OH and HCHO species simultaneously. The wavelength-tuned laser beam was expanded to thin laser sheet (its thickness is less than 0.4mm) by spherical lens and cylindrical lens, then exposed to the flames. For OH, a frequency doubled (532nm, 10Hz) Nd:YAG laser (GCR-230, Spectra Physics Inc.) pumped a Dye laser (HD-300, Lumonics Inc.) whose frequency was doubled to 283.2nm to excite the $Q_1(7)$ line of (1,0) band in $A^2\Sigma^+ \leftarrow X^2\Pi$ transition, ensuring that the fluorescence signal is less dependent on temperature [23]. The total energy per pulse was about 10 mJ. For HCHO, the third harmonic of a Nd:YAG laser (355 nm, PRO-230, Spectra Physics Inc.) was used to excite a weak rotational transition in the $AA_2 - XA_1 4_0^1$ vibronic manifold [24]. The pulse energy is 375 mJ. The calibration to determine absolute concentrations is conducted based on PLIF measurement and simulation of laminar flames. In our preliminary studies, it is confirmed that OH and HCHO fluorescence signals are proportional to these molar species concentrations [22,23], and the error is within 10%. On the other hand, orthogonal OH-PLIF measurements were applied to visualize the vertical plane by laser sheet 1 and horizontal plane by laser sheet 2. Since the same excitation line was used for both imaging, time delay of 100 ns was set to distinguish these fluorescence signals.

Fig.2

For the vertical imaging, two intensified CCD cameras with an array size of 1000 x 500 pixels were used. For OH signal, an interference filter centered at 307 nm (12 nm bandwidth) was placed in front of the

105-mm f/4.5 UV-Nikkor lens. For HCHO signal, a combination of a 395-nm high-pass and a 450-nm low-pass filter was used. Each capture area is 25 mm x 12.5 mm, and the spatial resolution is 25 $\mu\text{m}/\text{pixel}$. On the other hand, in horizontal plane, imaging area is 18.3 mm x 18.3 mm, and the corresponding pixel number is 680 x 680. The spatial resolution is about 27 $\mu\text{m}/\text{pixel}$. A set of 1000 images was obtained for statistical analysis.

Results and discussion

Turbulent burning velocity

Experimentally, we determined the turbulent burning velocity, S_T , which is the normal velocity of the mean flame cone of the time-averaged shape:

$$S_T = U_m \sin \theta \quad (2)$$

where θ is the mean apex angle of the flame cone. Here, we obtained S_T based on direct photographs of flames. **Figure 3** shows the variations of S_T/S_L^0 with u'/S_L^0 , where S_L^0 is the unstrained laminar burning velocity, and u' is the root-mean-square (rms) velocity fluctuation. As already mentioned, for $\phi_m = 0.75$, the global extinction occurs when the mean exit velocity is slightly above 30 m/s. Initially, S_T linearly increases with turbulence at $u'/S_L^0 < 2$. Then, the increasing rate starts to decrease. That is, the bending effect is observed. In the next session, we visualize the instantaneous flame structure.

Fig.3

Flame structure

Figure 4 shows HCHO and OH profiles in turbulent flames, which are simultaneous single-shot

fluorescence images. The conditions are for (a) $U_m = 10\text{m/s}$, $\phi_m = 0.75$, (b) $U_m = 30\text{m/s}$, $\phi_m = 0.75$, and (c) $U_m = 30\text{m/s}$, $\phi_m = 0.90$. It is known that HCHO exists mainly in the preheat zone whereas OH exists in relatively high temperature region in reaction zone and burned gas. As seen in **Fig. 4a**, there is one continuous flame front and the flame is wrinkled by turbulence. In **Fig. 4b**, the flame structure becomes more complex at higher exit velocity. Also, the width of HCHO region is thicker, corresponding to the thickened preheat zone in thin reaction zones regime [3]. OH region is distorted and collapsed, which could be local extinction. When equivalence ratio is larger at the same exit velocity in **Fig. 4c**, OH region is relatively smooth with its concentration higher.

Fig.4

Next, we examine the heat release rate based on the product of OH and HCHO concentrations. Results are shown in **Fig. 5**. At the mean exit velocity of 10 m/s in **Figs. 5a and 5b**, since the profile of heat release rate is continuous, it is considered that typical wrinkled laminar flames are formed. However, for $U_m = 30\text{m/s}$, $\phi_m = 0.75$ in **Fig. 5c**, the heat release rate becomes extremely low in a dotted circle. When the equivalence ratio is increased to 0.9 in **Fig. 5d**, the local extinction is seldom observed. Interestingly, the value of flame front that is convex to unburned gas is much smaller than that in the concave part. In case of lean propane/air mixtures, Lewis number is larger than unity. Thus, the above phenomena are explained by Lewis number consideration [7,10,11,19,25].

Fig.5

For further discussion, we investigated the variation of OH and HCHO concentrations in flames. In each PLIF image, the peak values of OH and HCHO concentrations obtained at $Z = 20$ mm were recorded and analyzed. **Figure 6** shows the frequency profile based on 1000 images. As for HCHO concentration, its concentration is higher at $\phi_m = 0.90$. As the mean exit velocity is increased, the profile becomes broadened, corresponding to the larger variation in concentration. As for OH concentration, these tendencies are the same, but in some cases for $U_m = 30\text{m/s}$ and $\phi_m = 0.75$, even peak OH concentration becomes zero. When there are not enough radicals in reaction region, the chain reaction may not be sustained, resulting in an incomplete

reaction or local quenching. Thus, as observed in **Fig. 5c**, the large reduction of OH in reaction zone occurs at local extinction where as HCHO concentration in preheat zone still remains.

Fig.6

We have focused on OH concentration in the flame region. It has been reported that the flame shape detected by OH-PLIF well corresponds to the flame front by simulation [26] or CH region [27]. Although the positions of peak OH and the maximum heat release rate are not the same [28], the flame structure can be discussed based on peak OH concentration [29]. **Figure 7** shows OH images in horizontal plane at different conditions. The sliced flame structures are well observed. As the mean exit velocity is increased, more wrinkling of the flame front is observed. Interestingly, at the lower equivalence ratio, the flame front could be distorted due to the turbulence. From the vertical and horizontal flame images in **Fig. 8**, it is confirmed that this disconnected flame region is not the pocket of isolated unburned gas or surrounding air but the local flame extinction.

Fig.7

Fig.8

As for the turbulence, there are positive and negative effects on the flame front. The former is that the flame surface area (A_T) is enlarged to increase the turbulent burning velocity. The latter is that A_T is reduced by the local flame extinction. To evaluate these effects, the flame perimeter is examined based on the 2D OH image in horizontal plane in **Fig. 7**. It may be noted that OH exists in both the flame zone and burned gas. Thus, using the threshold, the flame perimeter is calculated. The threshold value is 0.009 mol/m^3 , where the burning velocity determined by the peak OH concentration becomes zero [23]. Results are shown in **Fig. 9**. At the equivalence ratio of 0.9, the flame perimeter (L_f) is always increased as the mean exit velocity is higher. At the lower equivalence ratio of 0.75, L_f is increased until 20 m/s, but it is conversely smaller for $U_m > 20$ m/s.

Fig.9

Next, we try to estimate the flame surface area. We take following two steps. Firstly, the increasing ratio of R due to the flame wrinkling is obtained, which is the ratio of flame perimeter to the circle length of mean flame radius of R_f .

$$R = \frac{1}{1000} \sum_{k=1}^{1000} \frac{L_{f,k}}{2\pi R_{f,k}} \quad (3)$$

where k is the number of the image, R_f is the mean flame radius in each image. That is, R corresponds to the degree of flame wrinkling to enlarge the flame surface area. The mean flame radius is calculated using instantaneous OH image. Results obtained at $Z = 10, 20, 30, 40$ mm are shown in **Fig. 10**. Derivation bars show the maximum and minimum values. For both equivalence ratios, the increasing ratio of R is always larger than unity, and it is increased as the mean exit velocity is increased. It should be noted that this value is almost constant when the mean exit velocity and equivalence ratio are chosen.

Fig.10

Next, based on the axisymmetry, we calculate the flame surface area in the vertical plane. To consider the flame wrinkling in the vertical plane, multiplying it by R , the flame surface area is finally obtained in Eq. 4.

$$A_T = \frac{1}{1000} \sum_{k=1}^{1000} R \times 2\pi \int L_k(Z) dZ \quad (4)$$

where L is the radial location of flame front determined by the position of maximum heat release rate. The flame surface area is calculated based on the flame on the right hand side in **Fig. 5**. When multiple flamelets are observed at higher turbulence, this integration is conducted for all flames.

Results are shown in **Fig. 11a** for $\phi_m = 0.75$ and 0.90 to see the change of flame surface area with respect to the mean exit velocity, U_m . For comparison, turbulent burning velocity is shown in **Fig. 11b**, which is re-plotting of **Fig. 3**. First of all, the profile of **Fig. 11a** is not similar to that of the flame perimeter in **Fig. 9**.

Fig.11

That is, three-dimensional effects are substantial [15], and it is not appropriate to discuss the flame surface area based on 2D flame length. At the higher equivalence ratio, the flame surface area is smaller. Additionally, it is found that A_T is monotonically increased at the higher exit velocity, corresponding to the linear dependency to the turbulence [15,30]. However, the turbulent burning velocity in **Fig. 11b** can not increase linearly. If Eq. 1 is still valid, the local burning velocity must be decreased [23].

Therefore, we validate the formula proposed by Damköhler [1]. Results are shown in **Fig. 12**. The local burning velocity is estimated by the peak OH concentration [23,31], and the solid line shows the predicted value by Eq. 1. As seen in **Fig. 12**, it is found that the measured turbulent burning velocity is slightly lower. However, the difference is small. Therefore, the turbulence affects the local flame structure to decrease the local burning velocity, causing the bending in turbulent burning velocity. Thus, within the frame work in our measurement, the similar flamelet approach applied in wrinkled and corrugated flames could be still valid even in the thin reaction zones regime.

Fig.12

Conclusions

We have examined local flame structure by joint PLIF imaging, using simultaneous OH/HCHO PLIF and orthogonal OH-PLIF measurements. The cyclone-jet combustor is used to establish turbulent premixed flames for propane/air mixtures in a wide range of turbulence, covering the flamelet regime and thin reaction zones regime on combustion diagram. Following results are obtained.

- (1) As the mean exit velocity is increased, the instantaneous flame shape becomes complex, with multiple flamelets. Near the global extinction, there is a region where peak OH concentration in reaction zone becomes zero whereas HCHO concentration in preheat zone still remains. The large reduction of OH alters the flame structure with a decrease of heat release rate, resulting in the local extinction.

- (2) As for the turbulence, there are positive and negative effects on the flame front. The former is that the flame surface area (A_T) is enlarged to increase the turbulent burning velocity. The latter is that A_T is reduced by the local flame extinction. By considering the degree of flame wrinkling, three-dimensional flame surface area is obtained from 2D images. Different from the flame perimeter, A_T is linearly increased at the higher exit velocity, showing the substantial three-dimensional effects.
- (3) The turbulent burning velocity is firstly increased at larger mean exit velocity, but the bending effect is observed in the thin reaction zones regime. Since the turbulent burning velocity is well predicted by Damköhler's formula, the bending is explained by the reduction of local burning velocity. Thus, within the frame work in our measurement, the similar flamelet approach could be still valid even in the thin reaction zones regime.

Acknowledgments

The authors thank Mr. N. Hayashi and Prof. H. Yamashita of Nagoya University for very helpful discussions.

References

1. G. Damköhler, *Z. Elektrochem. Angew. Phys. Chem* **46** (1940) 601-626.
2. R. Borghi, in *Recent Advances in Aeronautics Science* (1985) 117-134.
3. N. Peters, *J. Fluid Mech.*, **384** (1999) 107-132.
4. S. Nishiki, T. Hasegawa, R. Borghi, and R. Himeno, *Proc. Combust. Inst.* **29** (2002) 2017-2022.
5. D. Bradley, M. Z. Haq, R. A. Hicks, T. Kitagawa, M. Lawes, C. G. W. Sheppard, and R. Woolley, *Combust. Flame* **133** (2003) 415-430.

6. N. Peters, *Proc. Combust. Inst.* **32** (2009) 1-25.
7. Y. Yahagi, T. Ueda, and M. Mizomoto, *Proc. Combust. Inst.* **24** (1992) 537-542.
8. G. I. Sivashinsky, *Proc. Combust. Inst.* **29** (2002) 1737-1761.
9. S. I. Yang and S. S. Shy, *Proc. Combust. Inst.* **29** (2002) 1841-1847.
10. S. Ishizuka and C. K. Law, *Proc. Combust. Inst.* **19** (1982) 327-335.
11. J. Sato, *Proc. Combust. Inst.* **19** (1982) 1541-1548.
12. F. T. C. Yuen, and Ö. L. Gülder, *Proc. Combust. Inst.* **32** (2009) 1747-1754.
13. M. Murayama, and T. Takeno, *Proc. Combust. Inst.* **22** (1988) 551-559.
14. Ö. L. Gülder, *Proc. Combust. Inst.* **31** (2007) 1369-1375.
15. Y. C. Chen, *Proc. Combust. Inst.* **32** (2009) 1771-1777.
16. H. Kido, M. Nakahara, K. Nakashima, and J. Hashimoto, *Proc. Combust. Inst.* **29** (2002) 1855-1861.
17. P. H. Paul, and H. N. Najm, *Proc. Combust. Inst.* **27** (1998) 43-50.
18. A. Fayoux, K. Zähringer, O. Gicquel, J. C. Rolon, *Proc. Combust. Inst.*, **30** (2005) 251-257.
19. B. O. Ayoola, R. Balachandran, J. H. Frank, E. Mastorakos, C. F. Kaminski, *Combust. Flame* **144** (2006) 1-16.
20. K. Yamamoto, Y. Nishizawa, and Y. Onuma, *JSME Int. J, Series B* **47-6** (2003) 408-415.
21. K. Yamamoto, et al., *Heat Transfer Asian Research*, **35** (2006) 501-512.
22. K. Yamamoto, et al., *Trans. Japan Society for Mechanical Eng.* **B73** (2007) 1943-1949.
23. K. Yamamoto, et al., *Proc. Combust. Inst.* **32** (2009) 1227-1235.
24. S. B. Dworkin, et al., *Proc. Combust. Inst.*, **32** (2009) 1311-1318.
25. K. Yamamoto, and S. Ishizuka, *JSME International Journal, Series B*, **46** (1) (2003) 198-205.
26. S. Gashi, J. Hult, K. W. Jenkins, N. Chakraborty, S. Cant, C. F. Kaminski, *Proc. Combust. Inst.* **30** (2005) 809-817.

27. M. Tanahashi, M. Murakami, G. Choi, Y. Fukuchi, T. Miyauchi, *Proc. Combust. Inst.* **30** (2005) 1665-1672.
28. S. Pfädler, F. Beyrau, A. Leipertz, *Optics Express* **15** (2007) 15444-15456.
29. H. Becker, P. B. Monkhouse, J. Wolfrum, R. S. Cant, K. N. C. Bray, R. Maly, W. Pfister, G. Stahl, and J. Warnatz, *Proc. Combust. Inst.* **23** (1990) 817-823.
30. S. Tachibana, J. Yamashita, L. Zimmer, K. Suzuki, A. K. Hayashi, *Proc. Combust. Inst.* **32** (2009) 1795-1802.
31. J. B. Bell, R. K. Cheng, M. S. Day, and I. G. Shepherd, *Proc. Combust. Inst.* **31** (2007) 1309-1317.

List of figure captions

Fig. 1 Cyclone-jet combustor.

Fig. 2 Joint PLIF Imaging system. Upper figure shows simultaneous OH and HCHO PLIF, and lower figure shows orthogonal OH PLIF in vertical and horizontal planes.

Fig. 3 Turbulent burning velocity as functions of rms velocity fluctuation for $\phi_m = 0.75$ and 0.9 .

Fig. 4 HCHO (upper) and OH (lower) fluorescence images.

Fig. 5 Product of fluorescence signals of OH and HCHO for (a) $U_m = 10\text{m/s}$, $\phi_m = 0.75$, (b) $U_m = 10\text{m/s}$, $\phi_m = 0.90$, (c) $U_m = 30\text{m/s}$, $\phi_m = 0.75$, and (d) $U_m = 30\text{m/s}$, $\phi_m = 0.90$.

Fig. 6 Frequency of peak concentrations of HCHO and OH at $Z = 20$ mm.

Fig. 7 OH-PLIF images in horizontal plane.

Fig. 8 OH images in (a) vertical plane, and (b) horizontal plane; $\phi_m = 0.75$, $U_m = 30\text{m/s}$.

Fig. 9 Variations of flame perimeter with mean exit velocity for $\phi_m = 0.75$ and 0.9 .

Fig. 10 The ratio of flame perimeter (L_f) to circle length of mean flame radius of R_f .

Fig. 11 Variations of (a) flame surface area, and (b) turbulent burning velocity with mean exit velocity for $\phi_m = 0.75$ and 0.9 .

Fig. 12 Turbulent burning velocity for $\phi_m = 0.75$ and 0.9 , compared with predicted value by Eq. (1).

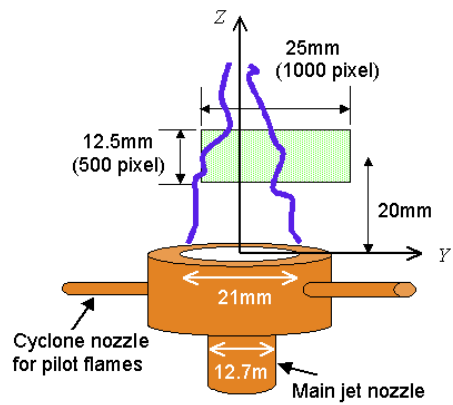


Fig. 1 Cyclone-jet combustor.

[Word Count] = (50+10)*2.2*1 + 4 (caption) = 136 words

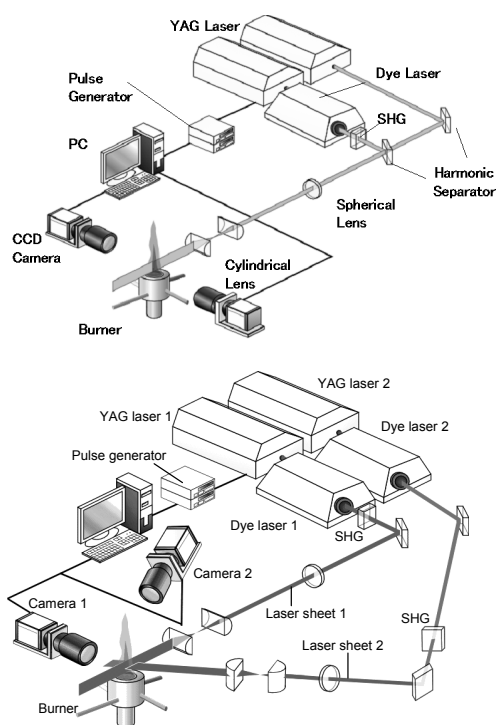


Fig. 2 Joint PLIF Imaging system. Upper figure shows simultaneous OH and HCHO PLIF, and lower figure shows orthogonal OH PLIF in vertical and horizontal planes.

[Word Count] = (95+10)*2.2*1 + 25 (caption) = 256 words

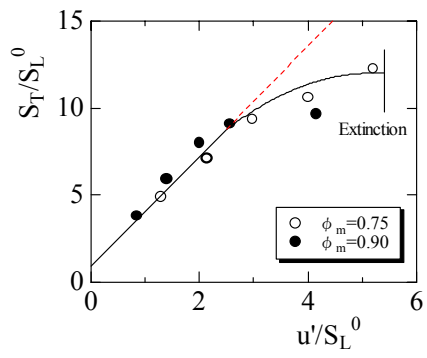
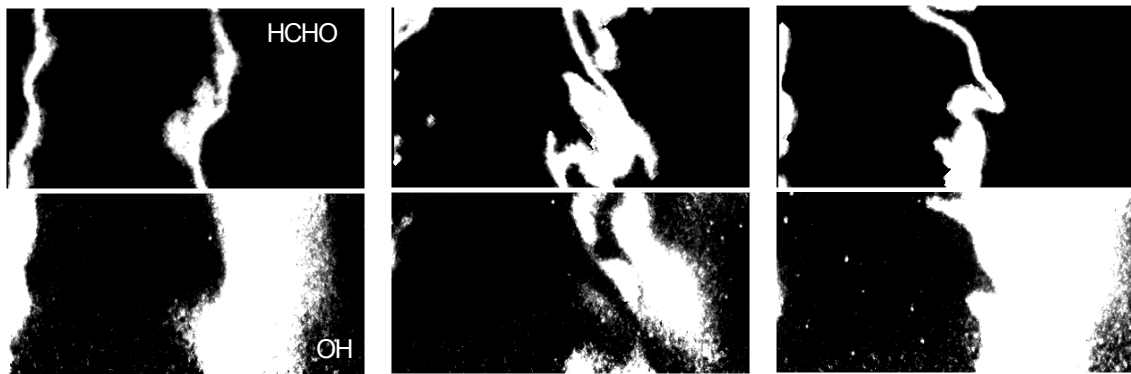


Fig. 3 Turbulent burning velocity as functions of rms velocity fluctuation for $\phi_m = 0.75$ and 0.9.

[Word Count] = (50+10)*2.2*1 + 17 (caption) = 149 words



(a) $U_m=10\text{m/s}$, $\phi_m=0.75$

(b) $U_m=30\text{m/s}$, $\phi_m=0.75$

(c) $U_m=30\text{m/s}$, $\phi_m=0.90$

Fig. 4 HCHO (upper) and OH (lower) fluorescence images.

[Word Count] = $(50+10)*2.2*2 + 9$ (caption) = 273 words

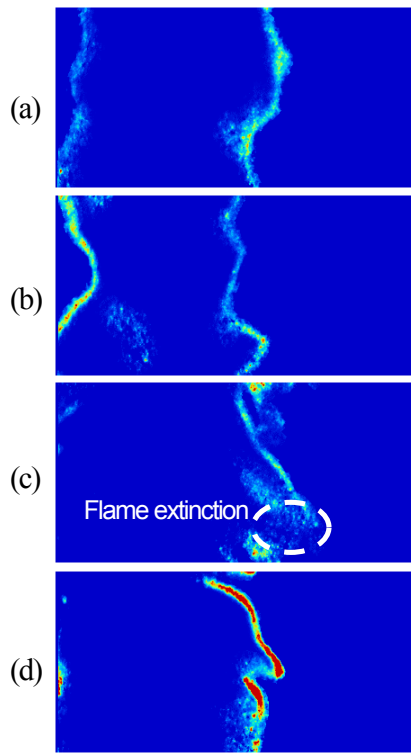


Fig. 5 Product of fluorescence signals of OH and HCHO for (a) $U_m=10\text{m/s}$, $\phi_m=0.75$, (b) $U_m=10\text{m/s}$, $\phi_m=0.90$, (c) $U_m=30\text{m/s}$, $\phi_m=0.75$, and (d) $U_m=30\text{m/s}$, $\phi_m=0.90$.

[Word Count] = $(98+10)*2.2*1 + 32$ (caption) = 270 words

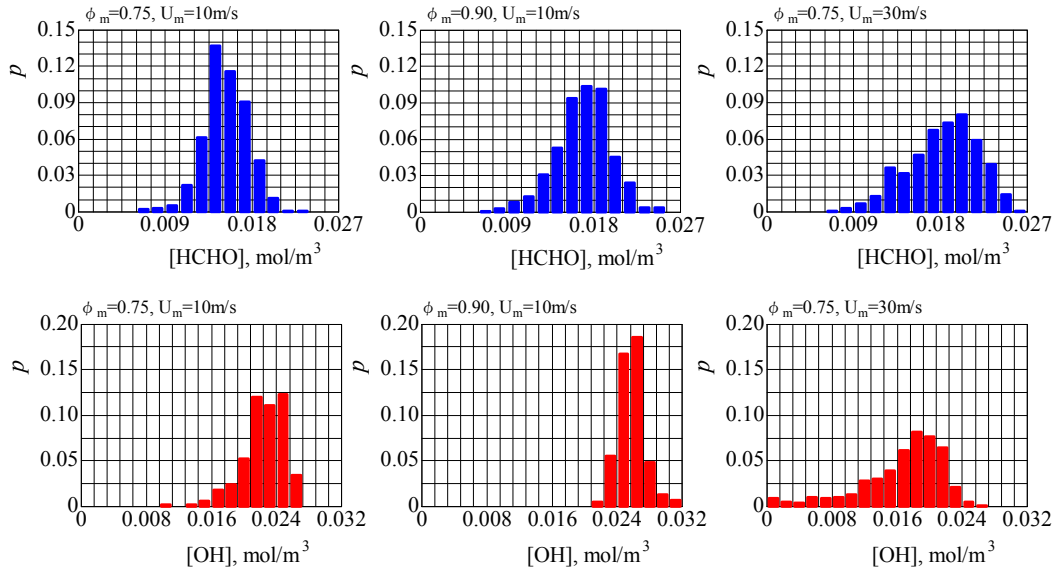


Fig. 6 Frequency of peak concentrations of HCHO and OH at $Z=20$ mm.

[Word Count] = $(75+10)*2.2*2 + 18$ (caption) = 381 words

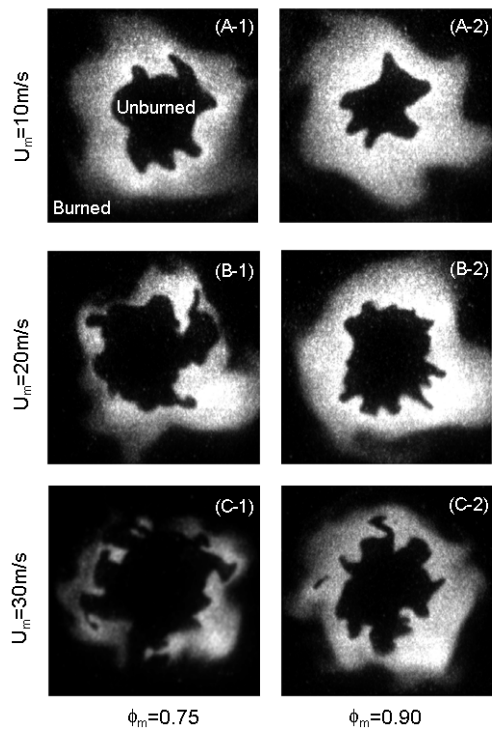


Fig. 7 OH-PLIF images in horizontal plane.

[Word Count] = $(95+10) \cdot 2.2 \cdot 1 + 7$ (caption) = 238 words

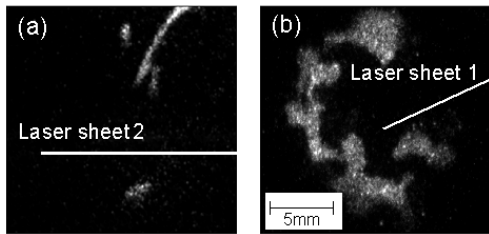


Fig. 8 OH images in (a) vertical plane, and (b) horizontal plane; $\phi_m=0.75$, $U_m=30\text{m/s}$.

[Word Count] = (30+10)*2.2*1 + 15 (caption) = 103 words

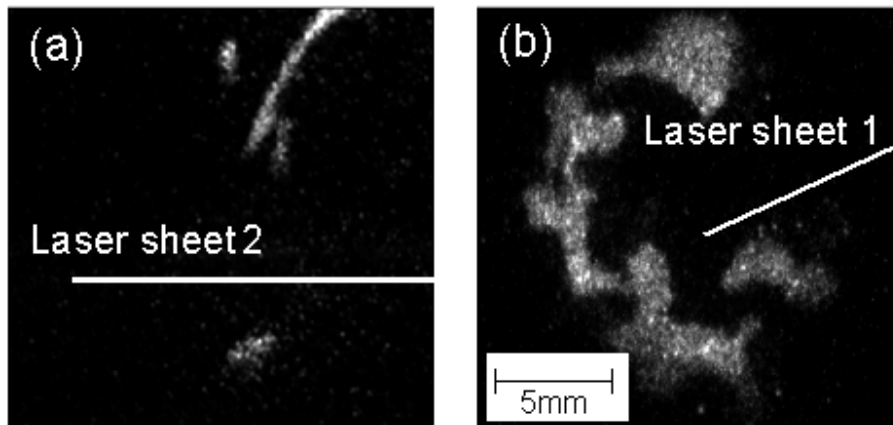


Fig. 8 (enlarged)

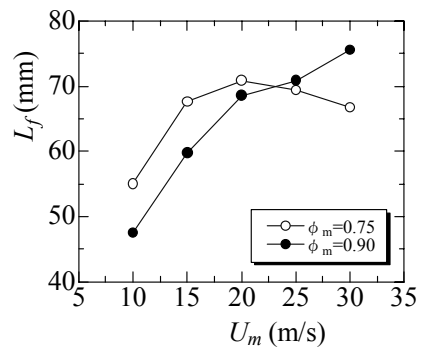


Fig. 9 Variations of flame perimeter with mean exit velocity for $\phi_m = 0.75$ and 0.9.

[Word Count] = (45+10)*2.2*1 + 16 (caption) = 126 words

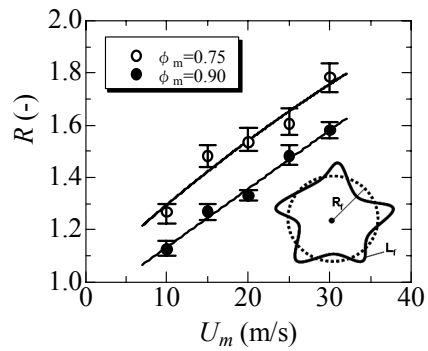


Fig. 10 The ratio of flame perimeter (L_f) to circle length of mean flame radius of R_f .

[Word Count] = (45+10)*2.2*1 + 19 (caption) = 140 words

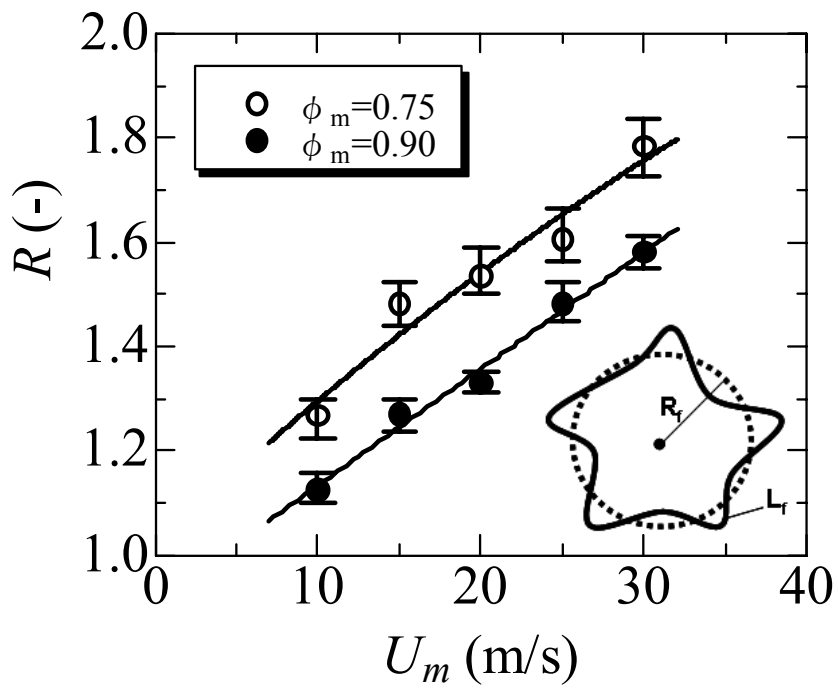


Fig. 10 (enlarged)

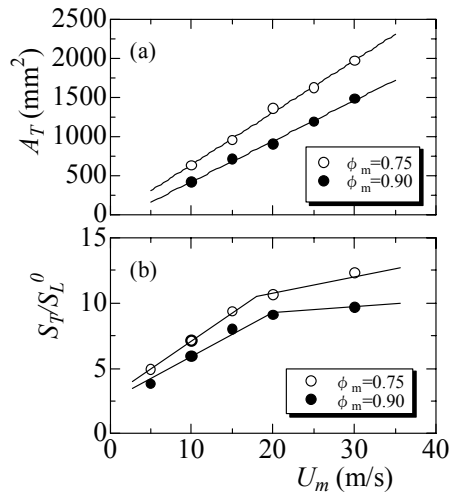


Fig. 11 Variations of (a) flame surface area, and (b) turbulent burning velocity with mean exit velocity for $\phi_m = 0.75$ and 0.9.

[Word Count] = (65+10)*2.2*1 + 23 (caption) = 188 words

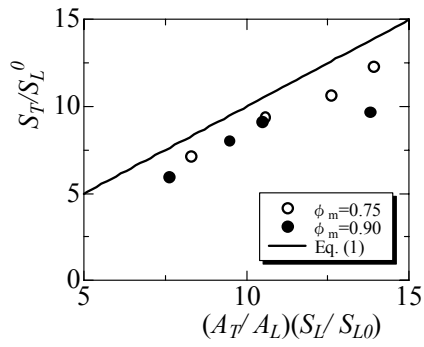


Fig. 12 Turbulent burning velocity for $\phi_m = 0.75$ and 0.9 , compared with predicted value by Eq. (1).

[Word Count] = $(45+10) \times 2.2 \times 1 + 18$ (caption) = 139 words